IEEE Photonics Journal
An IEEE Photonics Society Publication

Open Access

Automated Wavelength Alignment in a 4 × 4 Silicon Thermo-Optic Switch Based on Dual-Ring Resonators

Volume 10, Number 1, February 2018

Qingming Zhu
Xinhong Jiang
Yanping Yu
Ruiyuan Cao
Hongxia Zhang
Danping Li
Yanbo Li
Li Zeng
Xuhan Guo
Yong Zhang
Ciyuan Qiu

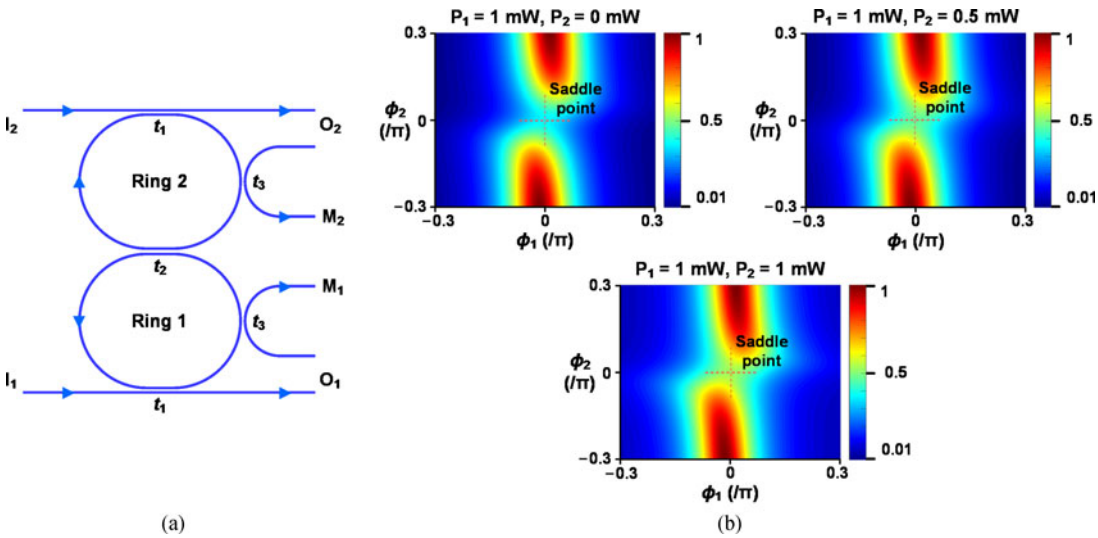

DOI: 10.1109/JPHOT.2018.2791561

Automated Wavelength Alignment in a 4 × 4 Silicon Thermo-Optic Switch Based on Dual-Ring Resonators

Qingming Zhu,[1] **Xinhong Jiang**,[1] **Yanping Yu**,[1] **Ruiyuan Cao**,[1] **Hongxia Zhang**,[1] **Danping Li**,[2] **Yanbo Li**,[2] **Li Zeng**,[2] **Xuhan Guo**,[1] **Yong Zhang**,[1] **and Ciyuan Qiu** [1]

[1]State Key Laboratory of Advanced Optical Communication Systems and Networks, Department of Electronic Engineering, Shanghai Jiao Tong University, Shanghai 200240, China
[2]Network Research Department, Huawei Technologies Co., Ltd., Shenzhen 518129, China

DOI:10.1109/JPHOT.2018.2791561

Manuscript received November 26, 2017; revised January 2, 2018; accepted January 5, 2018. Date of publication January 7, 2018; date of current version January 31, 2018. This work was supported in part by the National Natural Science Foundation of China under Grant 61505104/61605112, in part by the 863 High-Tech Program under Grant 2015AA015503, and in part by the Science and Technology Commission of Shanghai Municipality under Grant 16XD1401400/17500710900. Corresponding author: Ciyuan Qiu (e-mail: qiuciyuan@sjtu.edu.cn).

Abstract: We propose and experimentally demonstrate an automated resonance wavelength alignment scheme for an *O*-band 4 × 4 thermo-optic optical switch using dual-ring resonators. In this scheme, a new control algorithm based on saddle point searching is employed to align dual-input switching elements (SEs) and therefore the 4 × 4 switch. The proposed scheme is proven effective by demonstrating eight routing configurations for two 10-Gb/s data channels. The insertion losses of the three-stage SEs are ≤6.9 dB, and the crosstalk values are below −13.6 dB. Besides, the tolerance of the switch to the wavelength misalignment between the two optical input signals is measured. Negligible performance degradations are observed when the two channels are spaced by 0.05 nm.

Index Terms: Automated resonance wavelength alignment (ARWA), optical switching devices, resonators.

1. Introduction

To reduce the power consumption and footprints of large-scale switches, optical switching has emerged as a promising alternative to the conventional electrical switching [1], [2]. Optical switches based on various structures have been reported, such as Mach-Zehnder interferometers (MZIs) [3], [4], dual-ring assisted MZIs [5], nanobeam cavities [6], and micro-ring resonators [7]–[9]. In a typical optical switch design with multiple wavelength layers, each layer operates at a single wavelength [10], [11]. Therefore, resonator-based switches are attractive candidates as they exhibit lower power consumption and more compact device footprints [12], [13]. Furthermore, high-order resonators offer flat passband response and high out-of-band rejection, which are desired in switches employing multiple wavelengths [7], [14]. However, the resonance wavelengths of the resonator-based switches are highly susceptible to the fabrication variations and the chip temperature. Thus, thermo-optic (TO) tuning is often used to control the resonance wavelength. Applying such tuning method to large-scale switches requires effective automated resonance wavelength alignment (ARWA).

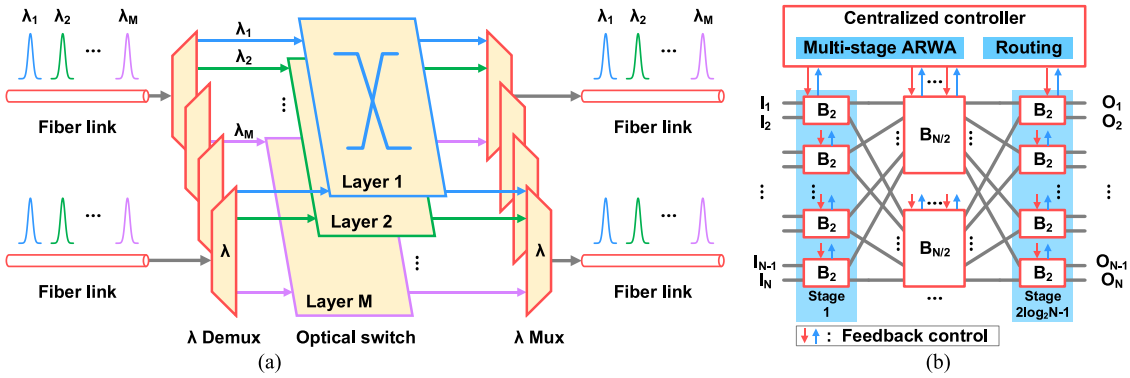

Fig. 1. (a) Typical WDM switching network architecture. (b) Schematic diagram of the single-wavelength N × N resonator-based switching layer. B_n is the $n \times n$ Benes network.

Multiple schemes have been proposed to realize the ARWA for first-order [15]–[19], second-order [14], and higher-order [20], [21] resonator based filters. The control algorithms used in previous ARWA schemes include dithering [15]–[17], homodyne locking [18], and maximum/minimum point searching [14], [19]–[22] techniques. However, these schemes are designed and demonstrated with single input signal, whereas a typical 2 × 2 switch operates with two input signals. The use of the second input signal can significantly change the transmission spectra of the 2 × 2 switch. To date, the ARWA for high-order resonators with two optical input signals has not been demonstrated.

In this paper, we propose an ARWA scheme for dual-input switching elements (SEs) using dual-ring resonators, and that is extended to a 4 × 4 switch. In the experiment, a 4 × 4 Benes architecture is used. The switch fabric consists of six switching elements (SEs) based on the dual-ring resonators. In the dual-ring resonator, the optical power at an integrated monitoring port as a function of the round-trip phase shifts of the two ring resonators is analyzed. The two-dimensional function does not follow the single-peak shape as in [14] but a saddle shape. A control algorithm based on saddle point searching (SPS) is then designed and employed in an off-chip thermal control sub-system to implement the ARWA. The feasibility of our scheme is verified by a proof-of-concept switching experiment, where the routing paths of two 10-Gb/s data channels can be simultaneously reconfigured on a fabricated 4 × 4 silicon photonic switch after the ARWA process. Eight routing configurations are demonstrated with a maximal insertion loss of the three-stage SEs of 6.9 dB, and the crosstalk values are below −13.6 dB. The 3-dB operation bandwidth of the 4 × 4 switch is 46 GHz at 1312.5 nm. The effects of wavelength misalignments between the two optical input signals are also evaluated. Negligible increases of the insertion loss and the crosstalk are observed when the misalignment is 0.05 nm, whereas a 1.0-dB additional insertion loss is induced and the maximal crosstalk value is −7.7 dB when the misalignment is 0.1 nm. Here, the 4 × 4 switch is designed to operate in O band for the switching applications in short reach communications.

2. Network Architecture and Sub-System Design

Fig. 1(a) shows a typical optical switching network architecture for wavelength division multiplexed (WDM) signals. Wavelength de-multiplexers and multiplexers are used so that the multiple-wavelength switching can be realized with multiple single-wavelength switching layers. In this paper, we mainly focus on realizing the single-wavelength switching layer using resonator-based devices, and the results can be further applied to multiple-wavelength switching networks. A schematic diagram of the single-wavelength N × N resonator-based switching layer is illustrated in Fig. 1(b), where Benes architecture is used because of the least number of 2 × 2 SEs to achieve all the N! routing configurations [4]. As can be seen in Fig. 1(b), $2\log_2 N - 1$ stages are used to construct the switch. A centralized controller is designed for realizing the multi-stage ARWA based on feedback

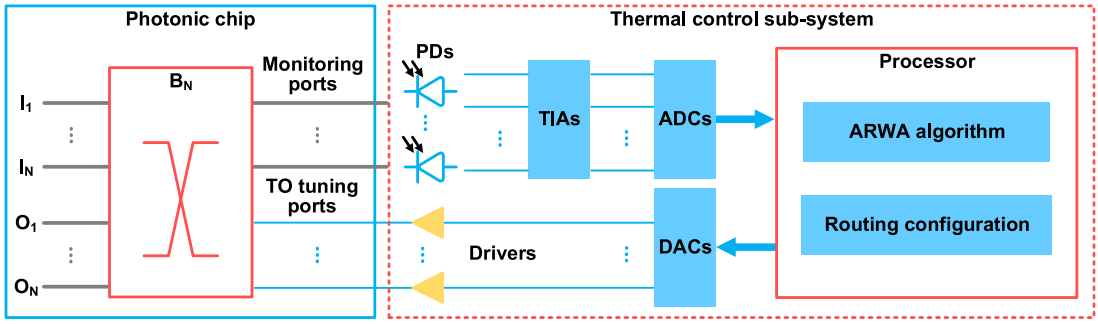

Fig. 2. Schematic diagram of the thermal control sub-system applied to the on-chip switch. PDs: photodetectors, TIAs: trans-impedance amplifiers, ADCs: analog-to-digital converters, DACs: digital-to-analog converters, TO: thermo-optic.

control and for routing all the SEs. The centralized control is desired for large-scale switches due to high robustness to the thermal disturbances [21].

The centralized controller in our scheme is implemented as a thermal control sub-system, with the schematic diagram shown in Fig. 2. In the sub-system, the optical signals at the monitoring ports of the switch are fed into photodetectors (PDs) for optical-to-electrical conversions. A trans-impedance amplifier (TIA) array is used for current-to-voltage conversions and amplifications. The output signals are then sampled by analog-to-digital converters (ADCs) and sent to a centralized processor. For the routing functionality of the Benes network implemented in the processor, effective routing methods have been proposed [23], [24]. In this paper, a $2^6 \times 6$ look-up table (LUT) is used for the routing configuration of a 4×4 Benes network. Based on the ARWA algorithm and the routing configuration, the resonance wavelengths of the SEs can then be controlled by the centralized processor through the TO tuning. In addition, there is possibility to reduce the ARWA cost in the Benes architecture with power monitors only in the last stage [22].

3. Operation Principle and Algorithm Design

In the thermal control sub-system, the ARWA sub-processes for the SEs in the same stage can be executed simultaneously, while the ARWA sub-processes for the cascaded SEs are executed in order. For all the SEs, the control algorithms are the same. Thus, we take the ARWA sub-process of a single SE to illustrate the operation principle. Fig. 3(a) shows the diagram of the SE, which consists of a dual-ring resonator while each race-track ring resonator has an integrated monitoring port by using a directional coupler.

In the dual-ring resonator, the transmission functions from I_1 to M_1 and M_2 are calculated using the transfer matrix method [25] and can be expressed as

$$T_{M1} = -k_1 k_3 a_1^{1/4} \frac{1 - t_1 t_2 t_3 a_2}{(t_1 t_3 a_1 - t_2)(t_1 t_3 a_2 - t_2) + k_2^2}, \tag{1}$$

$$T_{M2} = -jk_1 k_3 a_1^{1/2} a_2^{3/4} \frac{t_1 k_2 t_3}{(t_1 t_3 a_1 - t_2)(t_1 t_3 a_2 - t_2) + k_2^2}, \tag{2}$$

where t_i and k_i ($t_i^2 + k_i^2 = 1$, $i = 1, 2, 3$) are the transmission and coupling coefficients of the three directional couplers, respectively. $a_i = \exp(-\alpha L - j\phi_i)$ ($i = 1, 2$) is the transmission factor along Ring i, with L denoting the circumference of the ring resonators. α is the waveguide loss factor and $\phi_i = -2\pi n_g L\, \Delta\lambda_i / \lambda_0^2$ ($i = 1, 2$) is the round-trip phase shift of Ring i. n_g represents the waveguide group index. $\Delta\lambda_i$ is the misalignment between the resonance wavelength of Ring i and the operation wavelength λ_0. Therefore, $\phi_1 = \phi_2 = 0$ is satisfied when both Ring 1 and Ring 2 are resonant at λ_0.

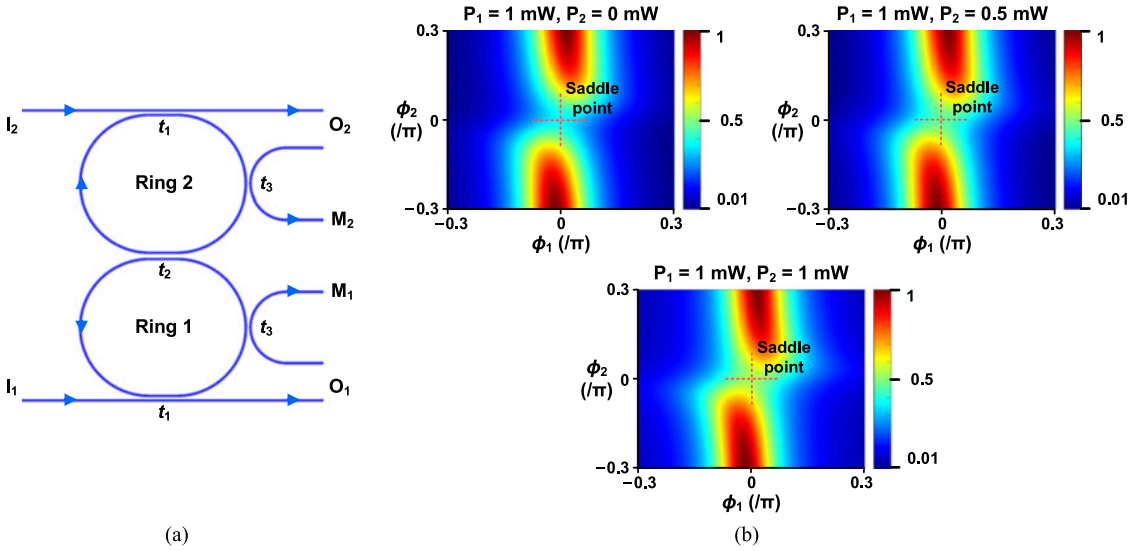

Fig. 3. (a) Schematic of the dual-ring structure in each SE. (b) Normalized $P_{M1}(\phi_1, \phi_2)$ for $P_1 \geq P_2$.

According to (1) and (2), when there are two uncorrelated lights fed into the device, the optical power P_{M1} of the monitored signal out of M_1 as a function of ϕ_1 and ϕ_2 can be written as

$$P_{M1}(\phi_1, \phi_2) = |T_{M1}E_1 + T_{M2}E_2|^2 = k_1^2 k_3^2 e^{-\alpha L/2} \frac{\left|e^{j\phi_2} - f_1\right|^2 P_1 + f_2^2 P_2}{\left|(e^{j\phi_1} - f_1)(e^{j\phi_2} - f_1) + f_2^2\right|^2},$$
$$f_1 = t_1 t_2 t_3 e^{-\alpha L},$$
$$f_2 = t_1 k_2 t_3 e^{-\alpha L}, \tag{3}$$

where E_i and P_i $(i = 1, 2)$ are the optical field and optical power of the light launched into I_i, respectively. To achieve a high extinction ratio of the transmission spectrum at the output ports and therefore low in-band crosstalk [26], [27], we carefully designed the dual-ring resonators based on a Matlab simulation, which calculates the transmission spectra at the output and monitoring ports by using the transfer matrix method [25]. The corresponding structural parameters of the fabricated dual-ring resonator are experimentally measured as follows: the transmission coefficients of the directional couplers are $t_1 = 0.801$, $t_2 = 0.976$, and $t_3 = 0.990$, and the waveguide transmission loss factor is $\alpha = 1.98\,\text{cm}^{-1}$. The radius of each ring resonator is $R = 10\ \mu$m. Then, we constructed and fabricated the 4×4 silicon TO switch using the dual-ring resonators with the same structural parameters. In the following discussion, we use the above parameters to perform the numerical calculations. Note that small deviations of these parameters would not affect the ARWA process.

If $P_1 \geq P_2$ is satisfied, normalized $P_{M1}(\phi_1, \phi_2)$ with different optical input powers are numerically calculated and shown in Fig. 3(b). It is observed that:

1) $P_{M1}(\phi_1)$ has a single local maximum for any ϕ_2;
2) $P_{M1}(\phi_2)$ has a single local minimum for any ϕ_1;
3) $P_{M1}(\phi_1, \phi_2)$ has a single saddle point at $\phi_1 = \phi_2 = 0$.

Consequently, to find the point where $\phi_1 = \phi_2 = 0$, a SPS process including the following steps is introduced:

Step 1. Tune ϕ_1 and find the local maximum of $P_{M1}(\phi_1)$. Note that $\phi_1 \approx 0$ at the local maximum point.
Step 2. Tune ϕ_2 and find the local minimum of $P_{M1}(\phi_2)$. Note that $\phi_2 \approx 0$ at the local minimum point.
Step 3. Repeat Steps 1 and 2 to minimize ϕ_1 and ϕ_2.

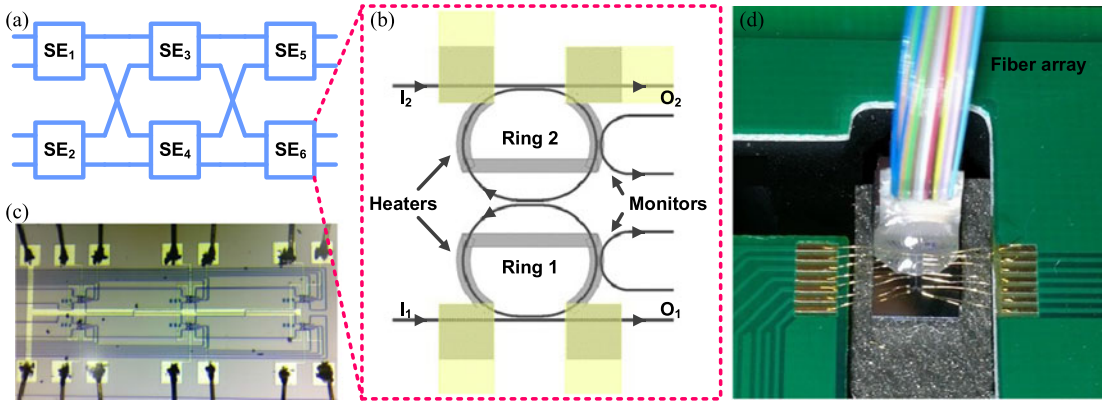

Fig. 4. (a) 4 × 4 Benes network. (b) Schematic of the 2 × 2 SE. (c) Micrograph of the fabricated 4 × 4 switch. (d) Photograph of the packaged switch chip.

Furthermore, owing to the symmetrical dual-ring structure, $P_{M2}(\phi_1, \phi_2)$ has a single saddle point at $\phi_1 = \phi_2 = 0$ when $P_1 < P_2$ is satisfied. Here, Ring i is defined as the master ring if the input power of I_i is higher than that of I_{3-i} ($i = 1, 2$), and the other ring resonator is the slave ring. Since there can be an optical input fed into either of the two input ports of the 2 × 2 SE or two inputs fed into both of them, the master ring can be either of the two ring resonators. The directional coupler in each ring resonator is therefore necessary for power monitoring. As a result, the monitored power of the master ring versus ϕ_1 and ϕ_2 is always subject to the saddle shape. Therefore, the point where $\phi_1 = \phi_2 = 0$ can be located by using a master ring identification process and the subsequent SPS process.

Based on the above principle, an ARWA algorithm for the 2 × 2 dual-ring resonator based switch is designed as follows:

Step 1. Apply a set of uniformly-distributed TO tuning powers to the two ring resonators simultaneously, and measure the corresponding monitored powers of the two ring resonators. The ring resonator with higher peak monitored power is set as the master ring. Note that once the master ring is identified, only a single power monitor is used in the following steps.

Step 2. Apply another set of uniformly-distributed TO tuning powers to the master ring, and measure the corresponding monitored powers of the master ring P_{master}. Set the master ring to operate at the state with the local maximal P_{master}.

Step 3. Apply the same set of powers as that in Step 2 to the slave ring, and measure the corresponding P_{master}. Set the slave ring to operate at the state with the local minimal P_{master}. Note that the ranges of the applied power sets in Steps 1−3 are large enough to find the resonance wavelengths.

Step 4. Repeat Steps 2 and 3 to minimize the misalignments between the resonance wavelengths and the operation wavelength.

In order to alleviate the thermal crosstalk effects, the ARWA sub-process of each SE and the ARWA process of the 4 × 4 switch are carried out for several iterations, thus minimizing the insertion losses and the crosstalks.

4. Device Design, Fabrication and Experimental Verifications

The switch fabric includes six 2 × 2 SEs, which form an on-chip 4 × 4 Benes network, as shown in Fig. 4(a). The schematic of the SE is provided in Fig. 4(b). Each SE consists of two coupled ring resonators, two ∼98:2 directional couplers for power monitoring and metal heaters for the TO tuning. The radius of the micro-ring resonators is 10 μm. The coupling gaps between the micro-ring resonators and the straight waveguides are 217 nm, and the coupling gap between the two

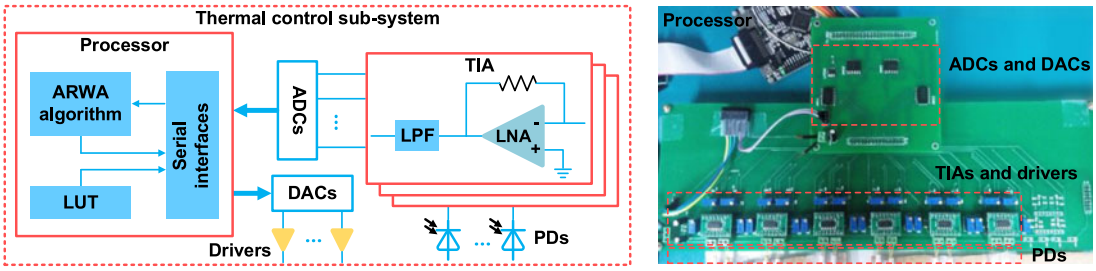

Fig. 5. (a) Setup of the thermal control sub-system. (b) Photograph of the thermal control sub-system. LNA: low-noise amplifier. LPF: low-pass filter. LUT: look-up table.

micro- ring resonators is 360 nm. Fig. 4(c) depicts the micrograph of the fabricated switch after wire bonding. The device was fabricated on a silicon-on-insulator (SOI) wafer with a 220-nm-thick top silicon layer. Rib waveguides with 440-nm width, 220-nm height and 90-nm slab thickness were used to construct the photonic circuit, so that the device structure can be extended to an electro-optic (EO) switch design. In the fabrication processes, E-beam lithography (EBL, Vistec EBPG 5200) was used to define the device pattern. The top silicon layer was then etched by an inductively coupled plasma (ICP) etching process. A 1-μm-thick SiO_2 layer was then deposited on the whole device by plasma enhanced chemical vapor deposition (PECVD). 100-nm-thick Ti heaters and 1-μm-thick Al pads were fabricated using EBL and lift-off processes. The footprint of the 4 × 4 switch is $3,472\,\mu\text{m} \times 2,425\,\mu\text{m}$. Fig. 4(d) shows the switch chip after electrical and optical packaging. A 24-channel 127-μm-pitch fiber array is mounted on the switch chip by using ultra-violet (UV) light curable adhesive. The fiber-to-chip coupling loss is around 6 dB.

The switch fabric is controlled by the thermal control sub-system. Given the aforementioned schematic diagram of the sub-system in Section 2, the implemented sub-system with the setup provided in Fig. 5(a) is characterized as follows. To control the 12 ring resonators in the 4 × 4 switch, there are 12 feedback circuits in the thermal control sub-system. In each feedback circuit, a commercial PD (PDCS986) shows responsivity of ∼0.8 A/W in O band. In the TIA unit, a low-noise amplifier (LNA) with a gain of $\sim 10^6$ V/A is placed before a 10-KHz low-pass filter (LPF). By this means, the following 10-bit ADC (TLC1543) samples the amplified electrical signal with ≥ 28-dB signal-to-noise ratio (SNR) when the optical input power is ≥ -46 dBm. The sampled data from the 12 ADC channels are then sent to a single-core processor (STM32F407VET6) running at 168 MHz. The ARWA algorithm implemented in the processor controls the six SEs in order by executing the aforementioned four-step algorithm in Section 3. After the ARWA process, the 64 × 6 LUT implemented in the processor controls the routing states. During the ARWA or LUT routing reconfiguration process, 12 control voltages calculated by the processor are applied to the Ti heaters to control the resonance wavelengths of the 12 ring resonators through 8-bit DACs (TLC5628) and TO drivers. Fig. 5(b) shows the photograph of the thermal control sub-system.

To observe the automated control process before the switching experiment, the thermal control sub-system is firstly applied to an individual SE with the same device structure and design parameters as that in the 4 × 4 switch. The setup of this measurement is shown in Fig. 6(a). Two continuous wave (CW) lights at 1312.5 nm from O-band lasers (Santec TSL-550 and Emcore 1688 A) are adjusted to be TE-polarized by polarization controllers (PCs) and subsequently injected into the 2 × 2 SE controlled by the thermal sub-system. The monitored signal P_{master} is detected by the sub-system and measured by an oscilloscope (Tektronix TBS1102). Before the ARWA algorithm starts, the initial resonance wavelengths of the ring resonators are ∼1311.5 nm with $P_{\text{master}} \approx 0$. After the master ring being identified, the following first ARWA iteration consists of maximum and minimum searching sub-processes, corresponding to Step 2 and Step 3 in the ARWA algorithm. The two steps are then iterated for two times to alleviate the thermal crosstalk effects. Fig. 6(b) plots the waveform of the measured P_{master} during the progress of one iteration of the control algorithm. The duration of each ARWA iteration is ∼3 ms.

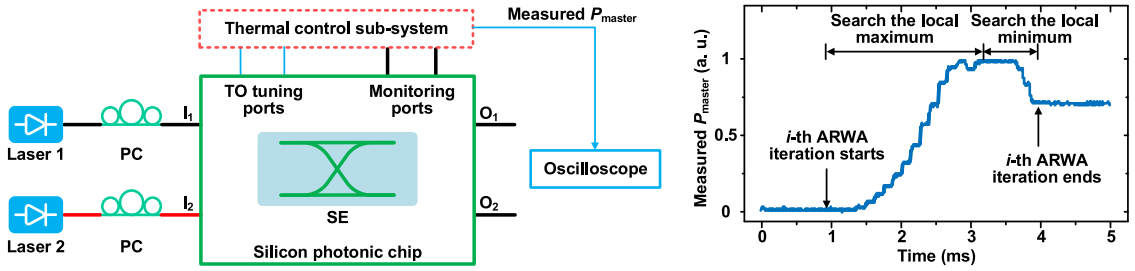

Fig. 6. (a) Experimental setup for measuring P_{master}. (b) Waveform of the measured P_{master} during the progress of one iteration of the control algorithm. PC: polarization controller.

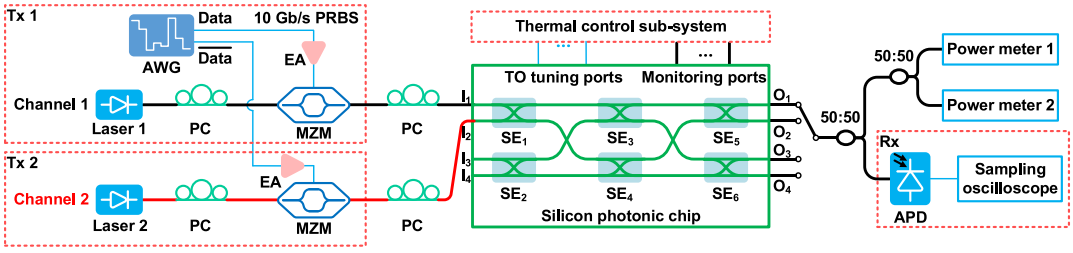

Fig. 7. Experimental setup for the 4 × 4 switch. PC: polarization controller. MZM: Mach-Zehnder modulator. AWG: arbitrary waveform generator. EA: electrical amplifier. APD: avalanche photodetector. The data signals of Channel 1 and Channel 2 are input to I_1 and I_2, respectively.

We then perform a proof-of-concept switching experiment to verify the feasibility of the proposed ARWA scheme for the 4 × 4 switch with two data channels. The experimental setup is illustrated in Fig. 7. At the transmitters, the two CW lights at 1312.5 nm are fed into two 25-GHz Mach-Zehnder modulators (MZMs) (FTM7939EK), respectively. Each MZM is biased at the quadrature point and modulated by a 10-Gb/s pseudo-random bit sequence (PRBS) data to produce an on-off-keying (OOK) signal. Here, a 25-GHz arbitrary waveform generator (AWG) (Keysight M8195A) is used to generate the PRBS signals at a pair of differential output ports, which are then amplified by electrical amplifiers (EAs). The data streams have the same word length of 2^{15} –1, due to the AWG memory limitation. The output signals of the MZMs are injected into the switch chip with the same input power of 0.4 dBm. On-chip optical signal switching is then achieved based on the thermal control sub-system. Next, a single receiver is used to measure one of the four output signals at a time. The received signal is split into three parts. The first one is detected by a ~7-GHz avalanche photodetector (APD). Due to the lack of an O-band optical amplifier, the low-speed APD is used to achieve a high receiver sensitivity, thus limiting the data rates. After the detection, the eye diagram of the electrical signal is tested by a 12.4-GHz sampling oscilloscope (Keysight 86100D). The second part is sent into a Labview-controlled power meter to obtain the transmission spectra, and the last part is used for real-time power monitoring.

For a 4 × 4 non-blocking Benes network, there are 24 routing configurations consisting of 32 different routing paths [4], [28]. However, due to fabrication errors of the metal heaters, only the resonance wavelengths of SE_1, SE_3 and SE_4 are reconfigurable. For SE_2, SE_5 and SE_6, their resonance wavelengths are ≤1311.6 nm while the operation wavelength is fixed at 1312.5 nm. With the experimentally measured Q factors of the dual-ring resonators being ~3800, SE_2, SE_5 and SE_6 therefore operate in the bar state, as observed in the corresponding transmission spectra. Thus, the feasibility of the proposed control algorithm is experimentally verified for eight of the 24 non-blocking routing configurations, as listed in Table 1. For each routing configuration, all the SEs operate in proper cross/bar states [29] at the operation wavelength, thus routing the two optical input signals to the designated output ports. Fig. 8 depicts the normalized transmission spectra for two of the eight routing configurations. In Configuration 1, all the SEs are set to the bar states

TABLE 1
Eight of the 24 Non-Blocking Routing Configurations of the 4 × 4 Switch

Configuration ID	Output ports		Switching states[a]					
	Channle 1	Channle 2	SE_1	SE_2	SE_3	SE_4	SE_5	SE_6
1	O_1	O_2	1	1	1	1	1	1
2	O_1	O_4	1	1	1	0	1	1
3	O_2	O_1	0	1	1	1	1	1
4	O_2	O_3	0	1	0	1	1	1
5	O_3	O_2	1	1	0	1	1	1
6	O_3	O_4	1	1	0	0	1	1
7	O_4	O_1	0	1	1	0	1	1
8	O_4	O_3	0	1	0	0	1	1

[a]"0" represents the cross state and "1" represents the bar state.

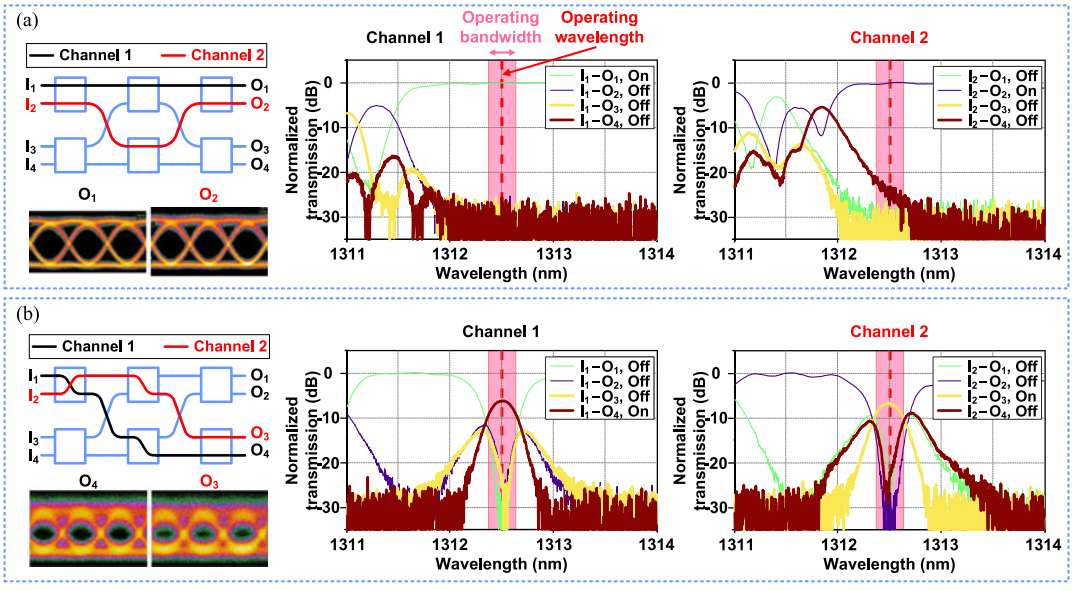

Fig. 8. Normalized transmission spectra for two of the eight routing configurations after the ARWA processes. (a) Configuration 1. (b) Configuration 8. The insets show the eye diagrams of the received signals.

without TO tuning power, and the corresponding resonance wavelengths are <1311.8 nm. By the automated TO tuning, SE_1, SE_3 and SE_4 are set to be resonant at the operation wavelength of 1312.5 nm to achieve the cross states, thus realizing Configuration 8. The available operation bandwidth of the 4 × 4 switch is 46 GHz, which is the minimal 3-dB bandwidth of all the measured routing channels. The degradations of the eye diagrams in Configuration 8 are mainly caused by the increased insertion loss and crosstalk, which limit the application of our ARWA scheme in larger switches. We believe that our ARWA scheme is possible to be applied in larger switch fabrics if the insertion losses are reduced with optimized fabrication processes and the crosstalk values are

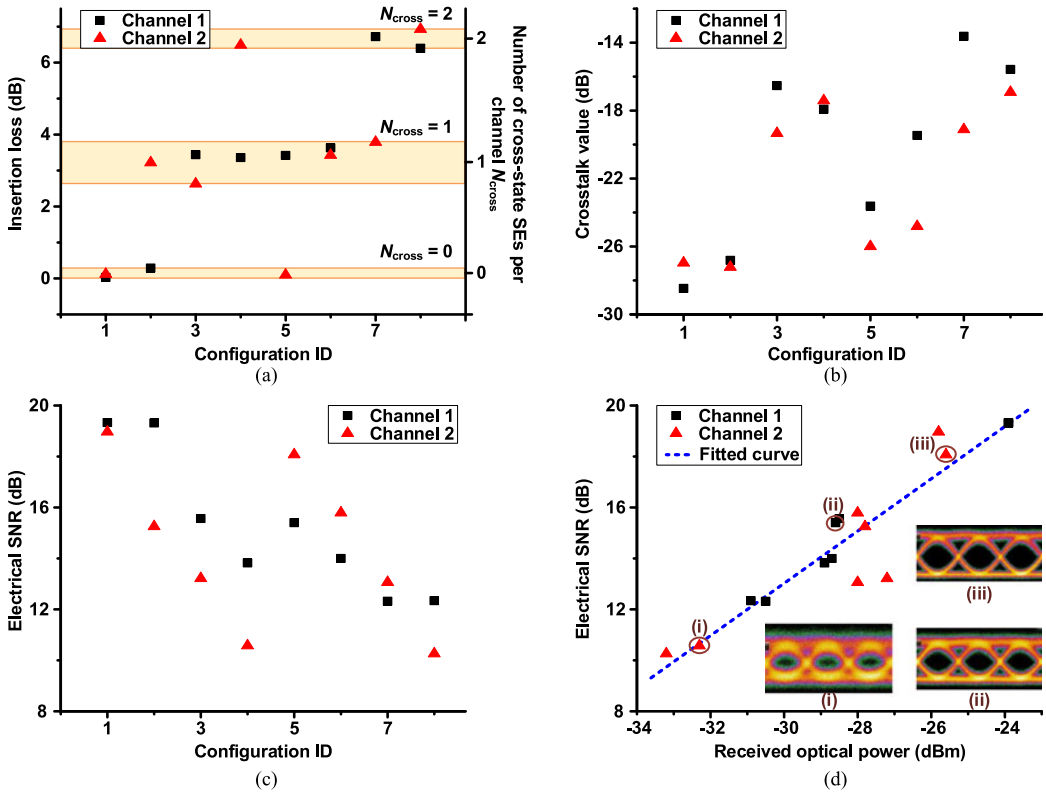

Fig. 9. Experimental results of the eight routing configurations after the ARWA processes. (a) Insertion losses of the three-stage SEs. (b) Crosstalk values. (c) Electrical SNRs. (d) Electrical SNR versus received optical power. SNR: signal-to-noise ratio.

reduced with mitigated thermal crosstalk effects by using a thermoelectric cooler (TEC). During the heating process, the experimentally measured thermal tuning efficiency is ~0.10 nm/ mW, which is designed to be ~0.15 nm/mW by a two-dimensional finite element method simulation for the heating process [30] and numerical calculations.

Then, for the two routing paths of the eight routing configurations, the insertion losses of the three-stage SEs and the crosstalks at the operation wavelength are calculated from the corresponding transmission spectra, as shown in Fig. 9(a) and (b). The insertion loss of each routing path exhibits a linear relationship with the number of cross-state SEs in the path N_{cross}, with an average insertion loss per cross-state SE of 3.3 dB. The maximal on-chip insertion loss of the switch fabric is 17.8 dB, with 6.9 dB loss from the SEs and 10.8 dB loss from the straight waveguides fabricated by EBL. As for the crosstalk of the routing path from I_i to O_j induced by the m-th input ($m \neq i$), it is defined as the ratio of the leaked output power $P_{m\to j}$ to the output power $P_{i\to j}$ [4], [31]. In this experiment, we measured the crosstalks of Channel 1 and Channel 2 induced by the signals fed into I_2 and I_1, respectively. It is observed that the maximal crosstalk value is −13.6 dB. The increased crosstalk is mainly induced by the increased insertion loss of the three-stage SEs and the thermal crosstalk effects. In Fig. 9(c), the electrical SNRs of the received signals are calculated from the eye diagrams using the following equation [32]:

$$\mathrm{SNR} = 20 \log \left(\frac{\mu_1 - \mu_0}{\sigma_1 + \sigma_0} \right), \tag{4}$$

where μ_i and σ_i represent the mean value and standard deviation of the eye level i ($i = 0, 1$), respectively. The measured electrical SNRs shown in Fig. 9(c) are also plotted in Fig. 9(d) versus the received optical powers with a fitted line. The fitting errors mainly result from the values of the received optical powers, which are not directly measured at the receiver but calculated from

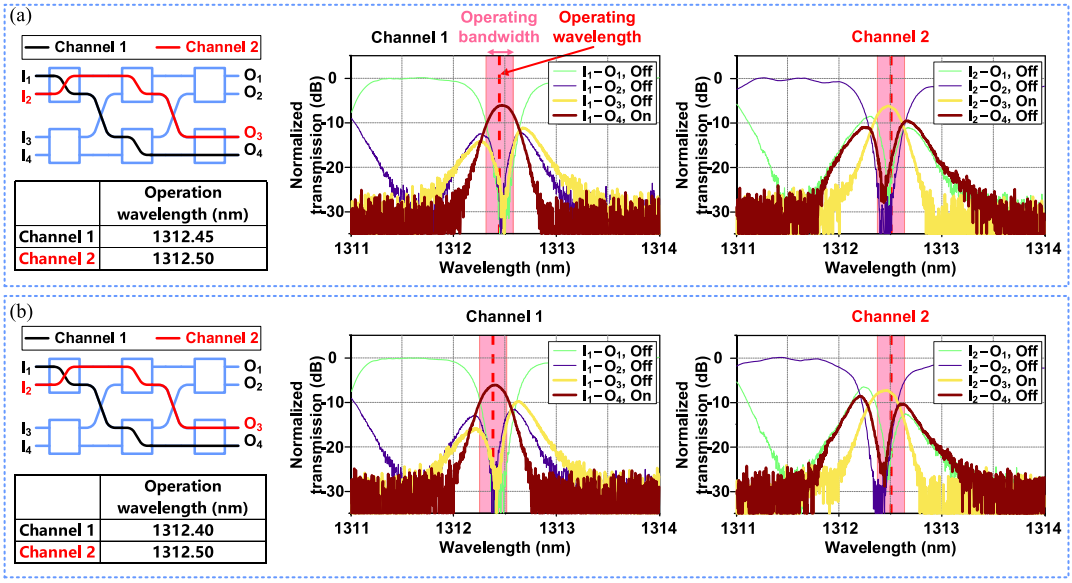

Fig. 10. Normalized transmission spectra for Configuration 8 after the ARWA processes (a) with 0.05-nm misalignment. (b) with 0.1-nm misalignment.

the transmission spectra. It is also found that σ_1 is larger than σ_0 for the measured eye diagrams, resulting from the in-band crosstalk effects [33].

A further testing on the tolerance of the thermally controlled switch fabric to the wavelength misalignment between the two input signals is carried out for Configuration 8, as depicted in Fig. 10. Compared to the misalignment-free case, the measured transmission spectra are similar to that in Fig. 8(b), but the resonance wavelengths of the SEs have been slightly detuned from each other. When the two lasers are spaced by 0.05 nm, negligible increases of the insertion loss and the crosstalk are observed. However, in the 0.1-nm misalignment case, an additional insertion loss of 1.0 dB is induced for Channel 2, and the maximal crosstalk values of Channel 1 and Channel 2 are -14.4 dB and -7.7 dB, respectively.

5. Conclusion

In summary, we have proposed and demonstrated a new control algorithm to realize the ARWA for dual-ring resonators with two input signals in a 4×4 silicon photonic switch. In this scheme, the monitored power of each SE versus the round-trip phase shifts of the two ring resonators is calculated and follows a saddle shape. A control algorithm based on SPS is therefore designed and experimentally demonstrated on our fabricated O-band 4×4 silicon TO switch employing the dual-ring resonators. Eight routing configurations are demonstrated for two 10-Gb/s data channels. For each routing configuration, the three-stage SEs are automatically set to proper cross/bar states based on the ARWA process, and $\leq$6.9-dB insertion losses of the three-stage SEs and ≤ -13.6-dB crosstalk values are achieved. The thermally controlled switch fabric exhibits a 46-GHz operation bandwidth, with tolerance to 0.05-nm operation wavelength misalignment between two different data channels.

Acknowledgment

The authors would like to thank the support of device fabrication by the Center for Advanced Electronic Materials and Devices of Shanghai Jiao Tong University.

References

[1] R. G. Beausoleil, P. J. Kuekes, G. S. Snider, S. Y. Wang, and R. S. Williams, "Nanoelectronic and nanophotonic interconnect," *Proc. IEEE*, vol. 96, no. 2, pp. 230–247, Feb. 2008.

[2] A. Shacham, K. Bergman, and L. P. Carloni, "On the design of a photonic network-on-chip," in *Proc. 1st Int. Symp. Netw.-Chip*, 2007, pp. 53–64.

[3] C. P. Chen *et al.*, "Programmable dynamically-controlled silicon photonic switch fabric," *J. Lightw. Technol.*, vol. 34, no. 12, pp. 2952–2958, Jun. 2016.

[4] L. J. Lu, L. J. Zhou, Z. X. Li, X. W. Li, and J. P. Chen, "Broadband 4 x 4 nonblocking silicon electrooptic switches based on Mach-Zehnder interferometers," *IEEE Photon. J.*, vol. 7, no. 1, Feb. 2015, Art. no. 7800108.

[5] L. J. Lu *et al.*, "4 x 4 silicon optical switches based on double-ring-assisted Mach-Zehnder interferometers," *IEEE Photon. Technol. Lett.*, vol. 27, no. 23, pp. 2457–2460, Dec. 2015.

[6] H. Y. Zhou *et al.*, "Compact, submilliwatt, 2 x 2 silicon thermo-optic switch based on photonic crystal nanobeam cavities," *Photon. Res.*, vol. 5, no. 2, pp. 108–112, Apr. 2017.

[7] H. L. R. Lira, S. Manipatruni, and M. Lipson, "Broadband hitless silicon electro-optic switch for on-chip optical networks," *Opt. Express*, vol. 17, no. 25, pp. 22271–22280, Dec. 2009.

[8] N. Sherwood-Droz *et al.*, "Optical 4x4 hitless silicon router for optical Networks-on-Chip (NoC)," *Opt. Express*, vol. 16, no. 20, pp. 15915–15922, Sep. 2008.

[9] R. Stabile, P. DasMahapatra, and K. A. Williams, "First 4x4 InP switch matrix based on third-order micro-ring-resonators," in *Proc. Opt. Fiber Commun. Conf.*, 2016, Paper Th1C.3.

[10] Y. J. Xiong, M. Vandenhoute, and H. C. Cankaya, "Control architecture in optical burst-switched WDM networks," *IEEE J. Sel. Areas Commun.*, vol. 18, no. 10, pp. 1838–1851, Oct. 2000.

[11] A. Deore, O. Turkcu, S. Ahuja, S. J. Hand, and S. Melle, "Total cost of ownership of WDM and switching architectures for next-generation 100Gb/s networks," *IEEE Commun. Mag.*, vol. 50, no. 11, pp. 179–187, Nov. 2012.

[12] B. G. Lee *et al.*, "Comparison of ring resonator and Mach-Zehnder photonic switches integrated with digital CMOS drivers," in *Proc. 23rd Annu. Meet. IEEE Photon. Soc.*, 2010, pp. 327–328.

[13] Y. Li, Y. Zhang, L. Zhang, and A. W. Poon, "Silicon and hybrid silicon photonic devices for intra-datacenter applications: State of the art and perspectives," *Photon. Res.*, vol. 3, no. 5, pp. B10–B27, Oct. 2015.

[14] H. Jayatilleka *et al.*, "Wavelength tuning and stabilization of microring-based filters using silicon in-resonator photoconductive heaters," *Opt. Express*, vol. 23, no. 19, pp. 25084–25097, Sep. 2015.

[15] K. Padmaraju, D. F. Logan, T. Shiraishi, J. J. Ackert, A. P. Knights, and K. Bergman, "Wavelength locking and thermally stabilizing microring resonators using dithering signals," *J. Lightw. Technol.*, vol. 32, no. 3, pp. 505–512, Feb. 2014.

[16] X. Z. Zheng *et al.*, "A high-speed, tunable silicon photonic ring modulator integrated with ultra-efficient active wavelength control," *Opt. Express*, vol. 22, no. 10, pp. 12628–12633, May 2014.

[17] X. L. Zhu *et al.*, "Fast wavelength locking of a microring resonator," *IEEE Photon. Technol. Lett.*, vol. 26, no. 23, pp. 2365–2368, Dec. 2014.

[18] J. A. Cox, A. L. Lentine, D. C. Trotter, and A. L. Starbuck, "Control of integrated micro-resonator wavelength via balanced homodyne locking," *Opt. Express*, vol. 22, no. 9, pp. 11279–11289, May 2014.

[19] E. Timurdogan *et al.*, "Automated wavelength recovery for microring resonators," in *Proc. Conf. Lasers Electro-Opt.*, 2012, Paper CM2M.1.

[20] J. C. C. Mak, W. D. Sacher, J. C. Mikkelsen, T. Y. Xue, Z. Yong, and J. K. S. Poon, "Automated calibration of high-order microring filters," in *Proc. Conf. Lasers Electro-Opt.*, 2015, Paper SW1N.2.

[21] J. C. C. Mak and J. K. S. Poon, "Multivariable tuning control of photonic integrated circuits," *J. Lightw. Technol.*, vol. 35, no. 9, pp. 1531–1541, May 2017.

[22] Y. Huang, Q. Cheng, N. C. Abrams, J. Zhou, S. Rumley, and K. Bergman, "Automated calibration and characterization for scalable integrated optical switch fabrics without built-in power monitors," in *Proc. 43rd Eur. Conf. Exhib. Opt. Commun.*, 2017, Paper M1A.3.

[23] Q. Cheng, M. Bahadori, and K. Bergman, "Advanced path mapping for silicon photonic switch fabrics," in *Proc. Conf. Lasers Electro-Opt., Sci. Innov.*, 2017, Paper SW1O. 5.

[24] Q. Cheng, M. Bahadori, Y. Huang, S. Rumley, and K. Bergman, "Smart routing tables for integrated photonic switch fabrics," in *Proc. 43rd Eur. Conf. Exhib. Opt. Commun.*, 2017, Paper M1A.2.

[25] A. Yariv, "Critical coupling and its control in optical waveguide-ring resonator systems," *IEEE Photon. Technol. Lett.*, vol. 14, no. 4, pp. 483–485, Apr. 2002.

[26] M. Bahadori *et al.*, "Crosstalk penalty in microring-based silicon photonic interconnect systems," *J. Lightw. Technol.*, vol. 34, no. 17, pp. 4043–4052. Sep. 2016.

[27] Y. Su *et al.*, "A multirate upgradeable 1.6-Tb/s hierarchical OADM network," *IEEE Photon. Technol. Lett.*, vol. 16, no. 1, pp. 317–319, Jan. 2004.

[28] M. S. Hai *et al.*, "Automated characterization of SiP MZI-based switches," in *Proc. Opt. Interconnect Conf.*, 2015, Paper TuP17.

[29] L. J. Lu, L. J. Zhou, S. L. Li, Z. X. Li, X. W. Li, and J. P. Chen, "4 x 4 nonblocking silicon thermo-optic switches based on multimode interferometers," *J. Lightw. Technol.*, vol. 33, no. 4, pp. 857–864, Feb. 2015.

[30] A. H. Atabaki, M. Soltani, S. Yegnanarayanan, A. A. Eftekhar, and A. Adibi, "Optimization of metallic micro-heaters for reconfigurable silicon photonics," in *Proc. Conf. Lasers Electro-Opt.*, 2009, Paper CThB.4.

[31] R. Jenkins *et al.*, "Novel 1× N and N× N integrated optical switches using self-imaging multimode GaAs/AlGaAs waveguides," *Appl. Phys. Lett.*, vol. 64, no. 6, pp. 684–686, 1994.

[32] N. S. Bergano, F. Kerfoot, and C. Davidsion, "Margin measurements in optical amplifier system," *IEEE Photon. Technol. Lett.*, vol. 5, no. 3, pp. 304–306, Mar. 1993.

[33] T. Gyselings, G. Morthier, and R. Baets, "Crosstalk analysis of multiwavelength optical cross connects," *J. Lightw. Technol.*, vol. 17, no. 8, pp. 1273–1283, Aug. 1999.